Engineering Structures 33 (2011) 1423–1438

Contents lists available at ScienceDirect

Engineering Structures

journal homepage: www.elsevier.com/locate/engstruct

Numerical modeling of ductile crack extension in high pressure pipelines with longitudinal flaws

Claudio Ruggieri *, Fernando Dotta

Department of Naval Architecture and Ocean Engineering, University of São Paulo, São Paulo, SP 05508-900, Brazil

ARTICLE INFO

Article history:
Received 8 July 2009
Received in revised form
6 September 2010
Accepted 4 January 2011
Available online 21 February 2011

Keywords:
Ductile fracture
Defect assessment
Pipelines
Computational cells
CTOA
Finite elements

ABSTRACT

This study examines the applicability of a micromechanics approach based upon the computational cell methodology incorporating the Gurson–Tvergaard (GT) model and the CTOA criterion to describe ductile crack extension of longitudinal crack-like defects in high pressure pipeline steels. A central focus is to gain additional insight into the effectiveness and limitations of both approaches to describe crack growth response and to predict the burst pressure for the tested cracked pipes. A verification study conducted on burst testing of large-diameter, precracked pipe specimens with varying crack depth to thickness ratio (a/t) shows the potential predictive capability of the cell approach even though both the GT model and the CTOA criterion appear to depend on defect geometry. Overall, the results presented here lend additional support for further developments in the cell methodology as a valid engineering tool for integrity assessments of pipelines with axial defects.

1. Introduction

Defect assessment procedures for high pressure piping systems play a key role in fitness-for-service analyses of oil and gas transmission pipelines, including onshore and offshore facilities. Common causes of failures in oil and gas transmission infrastructure derive primarily from crack-like surface flaws (either internal or external) that form during fabrication (slag and nonmetallic inclusions, weld cracks, lack of fusion, etc.) or during in-service operation (blunt corrosion, fatigue, stress corrosion cracking—SCC, dents at weld seams, etc.) [1–3]. As the pipeline infrastructure ages, robust procedures for integrity assessments become central to specifying critical flaw sizes which enter directly into procedures for repair decisions and life-extension programs of in-service structural components. Perhaps more importantly, these procedures must ensure fail-safe operations which avoid costly leaks and ruptures due to material failure to comply with the current stringent environment-based regulations.

A number of structural integrity procedures focus on axial flaws as these defects are subjected to high stresses due to internal pressure. Conventional failure criteria for longitudinal crack-like defects in pipelines are derived based upon a simple fracture mechanics analysis for planar or crack-like flaws. Such procedures are calibrated by extensive burst testing of pipes containing machined cracks conducted on low-to-moderate strength structural steels (API Grades X52 and X60) [4–6]. While these acceptance criteria for linepipe defects clearly simplify integrity analyses of in-service piping components, they essentially reflect a limit-load solution for a blunted axial crack in a pressurized vessel or pipe. Moreover, these integrity assessment procedures assume failure criteria which do not necessarily reflect the actual failure mechanism (such as, for example, stable crack growth prior to final failure) nor do they address specific requirements for high grade pipe steels currently used. For these cases, failure assessments may be overly conservative or provide significant scatter in their predictions, which lead to unnecessary repair or replacement of in-service pipelines at great operational costs [7].

Pressurized cracked pipelines made of high grade, high toughness steels often undergo significant stable crack growth prior to material failure. Under sustained ductile tearing of a macroscopic crack, large increases in the load-carrying (pressure) capacity for the flawed piping component are possible beyond the limits given by the pressure values at yielding of the remaining crack ligament. Simplified engineering approaches for defect assessments, such as the R6 [8], BS7910 [9], API579 [10] and SINTAP [11] methodologies, incorporate ductile tearing effects to evaluate the severity of crack-like flaws in structural components, including piping systems, in terms of the J-integral fracture parameter [12,13] to characterize the significant increase in toughness over the first few millimeters of stable crack extension (Δa). These methods, also referred to as engineering critical

* Corresponding author. Tel.: +55 11 30915184; fax: +55 11 30915717.
E-mail addresses: claudio.ruggieri@usp.br, claudio.ruggieri@gmail.com (C. Ruggieri).

0141-0296/$ – see front matter © 2011 Elsevier Ltd. All rights reserved.
doi:10.1016/j.engstruct.2011.01.001

assessment (ECA) procedures, rely on the direct application of crack growth resistance (J–Δa) curves (also often termed R-curves) measured using small laboratory specimens to the surface defects in pressure vessels and pipelines. However, laboratory testing of fracture specimens to measure resistance curves consistently reveals a marked effect of absolute specimen size, geometry, relative crack size (a/t) and loading mode (tension *vs.* bending) on R-curves (see [14,15] for illustrative examples). These effects observed in R-curves arise from the strong interaction between microstructural features of the material which govern the actual separation process and the loss of stress triaxiality in the crack front region due to large-scale yielding. Consequently, advanced methodologies for fracture assessments of pipelines must include robust procedures to transfer fracture resistance data measured using small laboratory specimens to structural piping components in engineering applications.

Current engineering methodologies to describe stable crack extension in ductile materials have developed essentially along two related lines of investigations incorporating local criteria: (1) micromechanics models which couple macroscale features of crack growth with the dominant microscale damage (material softening) of common structural steels and aluminum alloys, such as void nucleation, growth and coalescence [16–27] and (2) deformation-based approaches to control crack extension based upon a macroscopic measure of near-tip stresses and strains, such as the J-integral and the Crack Tip Opening Displacement (CTOD, δ), or, equivalently, the Crack Tip Opening Angle (CTOA) [28–33]. A widely used approach along with the first line of investigation utilizes the computational cell model proposed by Xia and Shih [21,22] to describe the macroscopic fracture resistance (J–Δa) based upon microstructural features and the flow properties for the material. In their model, a simplified form of the Gurson–Tvergaard (GT) constitutive model [23,24] for dilatant plasticity predicts microscopic void growth within a layer of elements (cells) of height $\approx\delta_{Ic}$ (the value of CTOD at onset of stable crack growth) defined over the remaining crack ligament; ductile crack extension occurs through cell extinction within this thin layer of material ahead of the crack tip. In contrast, the deformation-based approach employs a macroscopic growth parameter, most commonly the CTOA; crack extension occurs when the CTOA reaches a specified, critical value at a prescribed distance behind the crack tip.

The computational cell methodology has proven effective to quantify effects of geometry and loading mode on crack growth resistance curves for fracture specimens and structural components with relatively thick sections. These crack configurations develop high levels of stress triaxiality at the crack front which are required to drive the damage process of void growth and coalescence within the cells. However, the GT constitutive model upon which the cell methodology is based fails to describe adequately void growth under low constraint conditions which arise in thin section materials and tension loaded configurations. Engineering structures falling into this category include pressurized piping systems with surface flaws that form during fabrication or during in-service operation. These crack configurations generally develop low levels of crack tip stress triaxiality (associated with the predominant tensile loading which develops in pressurized piping systems) thereby raising concerns on the robustness of the GT-based cell model to predict crack growth followed by burst failure. An alternative approach involves the use of the deformation-based CTOA criterion to describe crack extension in low constraint structural components. While a number of researchers [31–33] have advanced the concept of the CTOA as a viable growth criterion for structurally thin panels and fracture specimens, application of the CTOA criterion to describe ductile tearing in thin-walled pipelines with surface flaws remains untested. The collective evidence at present from a wide range of studies reveals an uncertain picture of the predictive capability of the previous micromechanics models to describe ductile crack growth in cracked pipelines.

This study explores the capability of a micromechanics approach based upon the computational cell methodology incorporating the GT model and a deformation-based approach using the CTOA criterion to describe ductile crack response of longitudinal crack-like defects in high pressure pipeline steels. The present work builds upon previous analyses conducted by Dotta and Ruggieri [34] to predict the burst of a high pressure pipeline using a micromechanics model. A central focus is to gain additional insight into the effectiveness and limitations of both approaches to describe crack growth response while, at the same time, extending the methodology to a full 3-D framework. Laboratory testing of an API 5L X60 steel at room temperature using standard, deeply cracked fracture specimens provides the data needed to measure the crack growth resistance curve and to calibrate the GT and the CTOA parameters for this material. By interpreting these parameters in a phenomenological manner, they are assumed fixed in the analyses and then employed to predict experimentally measured burst pressures for thin-walled gas pipeline containing longitudinal cracks. The experimental program includes precracked pipe specimens with 508 mm (20 in) O.D. and varying crack depth to thickness ratios (a/t). Plane-strain and 3-D computations are conducted on detailed finite element models for the pipe specimens to describe crack extension with increased pressure. The article concludes by examining the significance of some numerical details and key parameters on the ductile tearing response which have a direct bearing on the predicted pressure values for the tested pipe specimens.

2. Overview of numerical modeling for ductile crack growth

2.1. Computational cell model for ductile tearing

This section presents a brief synopsis of the cell-based framework to model stable crack growth in ductile materials. Early experimental studies demonstrated the key role played by microvoid mechanisms on ductile fracture in metals (see, e.g., the review of Garrison and Moody [35]). Microvoids nucleate at inclusions or second-phase particles, either by decohesion of the particle-matrix interface or by fracture of the particles. Under increased deformation, these microvoids grow until localized plastic flow and necking of the ligament between adjacent microvoids (coalescence of microvoids) create a continuous fracture path (most often assisted by the rapid growth and coalescence of secondary microvoids). Fig. 1(a) pictures the schematic path of a Mode I growing crack in a ductile material. The material layer enveloping the growing crack, which must be thick enough to include at least a void or microcrack nucleus, identifies a process zone for the ductile fracture which conveniently gives the necessary length dimension for the model. Void growth and coalescence in the layer will cause the surface tractions that the process zone exerts on its surrounding drop to zero (this implicitly defines a traction–separation law for the process zone layer) thereby creating new fracture surfaces.

Motivated by the above observations, Xia and Shih (X&S) [21,22] proposed a model using computational cells to include a realistic void growth mechanism, and a microstructural length-scale physically coupled to the size of the fracture process zone. Void growth remains confined to a layer of material symmetrically located about the crack plane, as illustrated in Fig. 1(b), and having thickness D, where D is associated with the mean spacing of the larger, void initiating inclusions. This layer consists of cubical cell elements with dimension D on each side; each cell contains a cavity of initial volume fraction (the initial void volume divided

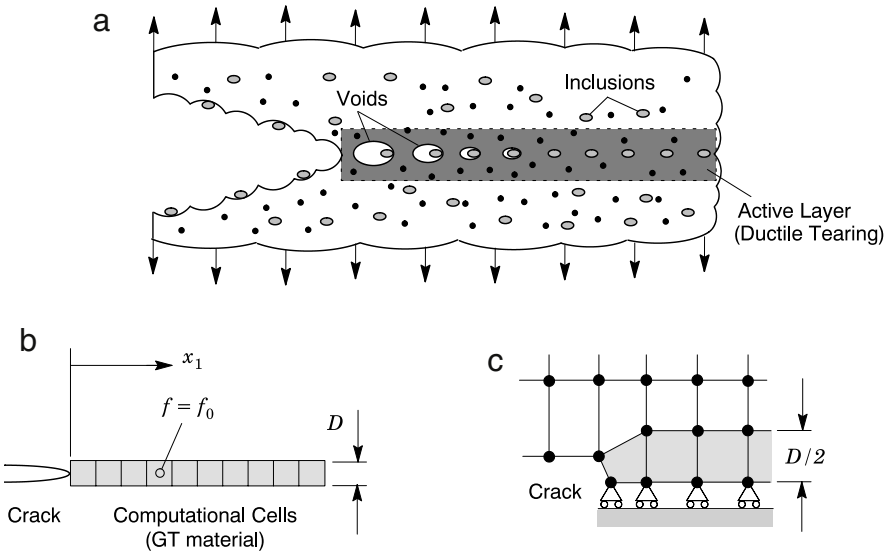

Fig. 1. Model for ductile crack growth using computational cells [21,26].

by cell volume). As a further simplification, the void nucleates from an inclusion of relative size immediately upon loading. Progressive void growth and subsequent macroscopic material softening in each cell are described with the Gurson–Tvergaard (GT) constitutive model for dilatant plasticity [23,24] given by

$$g(\sigma_e, \sigma_m, \bar{\sigma}, f) = \left(\frac{\sigma_e}{\bar{\sigma}}\right)^2 + 2q_1 f \cosh\left(\frac{3q_2\sigma_m}{2\bar{\sigma}}\right) - (1 + q_3 f^2) = 0 \quad (1)$$

where σ_e denotes the effective Mises stress, σ_m is the mean stress, $\bar{\sigma}$ is the current flow stress of the cell matrix material and f defines the current void fraction. Under multiaxial stress states, $\sigma_e = (3S_{ij}S_{ij}/2)^{1/2}$ where S_{ij} denotes the deviatoric components of Cauchy stress. Factors q_1, q_2 and $q_3 = q_1^2$ introduced by Tvergaard [24] improve the model predictions for periodic arrays of cylindrical and spherical voids. Values of $q_1 = 1.5$, $q_2 = 1.0$ in accord with [24] are often adopted. However, Faleskog et al. [25] have recently conducted a series of numerical analyses to determine values of q_1 and q_2 for varying material flow properties which improve cell model predictions of material softening behavior.

The GT yield function in Eq. (1) does not model realistically the rapid loss of stress capacity for larger void fractions nearing coalescence levels, nor does the model create new traction free surfaces to represent physical crack extension. In the present work, the evolution of stress within cells follows the original constitutive model of GT in Eq. (1) until $f = f_E$, where f_E typically has a value of 0.15–0.25; such a range of f_E-values does not alter the extinction process nor does the crack advance in the numerical model for large volume fractions ($f_E > 0.15$) as evident from the results shown in Section 7. Here, we adopt $f_E = 0.2$. The final stage of void linkup with the macroscopic crack front then occurs by reducing the remaining stresses to zero in a prescribed manner. Tvergaard [24] refers to this process as the element extinction or vanish technique. When f in the cell incident on the current crack tip reaches a critical value, f_E, the computational procedure removes the cell thereby advancing the crack tip in discrete increments of the cell size. The equivalent nodal forces associated with the remaining stresses are released over a specified number of subsequent load steps, denoted as N_{rs}; the number of release steps is usually assigned a value of 10 in typical numerical analyses. Zhang et al. [36] provide further discussion on the void coalescence mechanism and associated effects on ductile fracture response described by the Gurson constitutive model.

Fig. 1(c) shows the typical, plane strain finite element representation of the computational cell model where symmetry about the crack plane requires elements of size $D/2$ to maintain an arrangement of cubical cell elements (because of symmetry, each cell of size D is divided into four squared sub-elements of size $D/2$—see Fig. 1(b)). Material outside the computational cells, the "background" material, follows a conventional flow theory of plasticity and remains undamaged by void growth in the cells. Material properties required for this methodology include: for the background material, Young's modulus (E), Poisson's ratio (ν), yield stress (σ_{ys}) and hardening exponent (n) or the actual measured stress–strain curve; and for the computational cells: D and f_0 (and of much less significance f_E). The background material and the matrix material of the cells generally have identical flow properties. Using an experimental R-curve obtained from conventional fracture specimens, a series of finite element analyses of the specimen are conducted to calibrate values for the cell parameters D and f_0 which bring the predicted crack growth resistance curve into agreement with the experiment. Experience with plane-strain finite element analyses of fracture specimens to estimate D and f_0 for common structural and pressure vessel steels suggests values of 50–200 μm for D [26].

2.2. Crack extension using the CTOA criterion

Crack growth modeling approaches based upon macroscopic levels of deformation, such as J, CTOD or CTOA, retain contact with traditional fracture mechanics and provide a suitable framework to describe crack extension and instability during the fracture process. In particular, models based on the CTOA concept attain particular relevance here as it provides a viable and convenient growth criterion for low constraint crack configurations such as fracture specimens and structural components made of thin materials [31–33]. CTOA-controlled crack growth operates by advancing the crack front a prescribed distance when the CTOA reaches a critical value, θ_R. A key assumption of the methodology lies in the adoption of a constant value of CTOA during stable crack growth. A number of experimental observations (see review by Newman et al. [33]) support the use of a constant CTOA from the onset of ductile tearing in numerical analyses of crack extension for ductile materials.

Fig. 2 provides the essential features of the CTOA approach to describe ductile crack growth in a 2-D finite element setting.

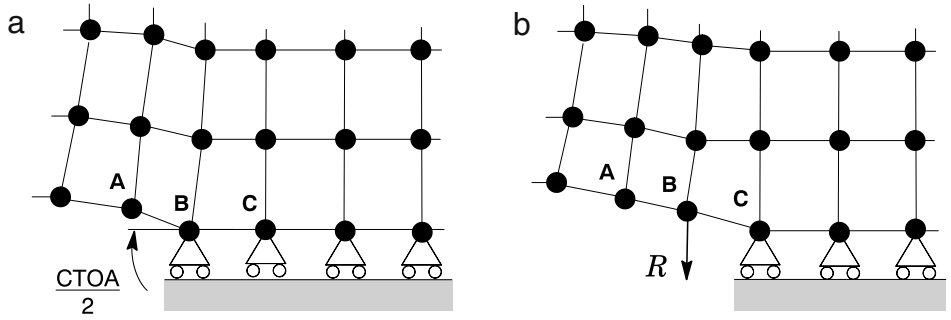

Fig. 2. Model for ductile crack growth using the CTOA criterion [31].

Fig. 2(a) shows the deformed mesh of the upper-half plane before crack advancement by node release. Symmetry conditions are enforced along the crack plane. Nodes unconstrained on the crack plane define the crack front whereas constrained nodes define the remaining ligament. The crack tip node and the nearest unconstrained node to the crack tip define the two points required to calculate the local CTOA value. Crack extension occurs when the local opening angle computed at a crack front node reaches the critical CTOA value. However, two critical CTOA values for growth need to be specified: (1) the initiation angle which controls crack extension over the near-tip blunting region defined by the node on the initial crack tip, and (2) the release angle which controls stable crack growth over the remaining nodes defining the crack ligament. Previous experimental and numerical studies [28–33] support the adoption of a higher value for the critical CTOA at crack initiation (see also Section 5.1 next).

A node release technique illustrated in Fig. 2(b) removes the constraint in the direction normal to the crack plane for the current crack tip node. Similarly to the cell extinction procedure adopted in the previous methodology, the corresponding node reaction is reduced gradually to zero in subsequent load increments, N_{rs}, to avoid numerical difficulties. Further details on the numerical implementation of the CTOA approach are provided by Gullerud et al. [31].

3. Finite element procedures

3.1. Numerical models for $C(T)$ fracture specimens

Nonlinear finite element analyses are conducted on a deeply cracked ($a/W = 0.5$) compact $C(T)$ fracture specimen with thickness $B = 13$ mm (0.5-T). Here, a denotes the crack length and W is the specimen width. Silva [37] measured tearing resistance curves in terms of J vs. Δa for an API X60 pipeline steel on this fracture specimen as described in Section 4. Fig. 3(a) shows the finite element model constructed for the plane-strain analyses of the tested deeply cracked 0.5-T $C(T)$ specimen. Symmetry conditions permit modeling of only one-half of the specimen with appropriate constraints imposed on the remaining ligament. The half-symmetric model has one thickness layer of 1078 8-node, 3-D elements with plane-strain constraints imposed ($w = 0$) on each node. Displacement controlled loading applied at the pin hole indicated in Fig. 3(a) enables continuation of the analyses once the load decreases during crack growth. To simulate ductile crack extension using the GT model, the finite element mesh contains a row of 130 computational cells along the remaining crack ligament ($W - a$) in a similar arrangement as shown in Fig. 1(b)–(c). The initially blunted crack tip accommodates the intense plastic deformation and initiation of stable crack growth in the early part of ductile tearing. To simulate ductile crack extension using the CTOA approach, initially squared-shaped elements are defined along the crack plane over which crack extension takes place. The use of square elements at the crack tip (with no initial crack tip blunting) simplifies computation of the initiation angle which precedes stable crack growth.

3-D finite element analyses are also conducted on a numerical model for the tested compact fracture specimen described previously. These analyses are employed to calibrate the cell parameter in a 3-D framework needed to predict the failure pressure for the axially cracked pipes described next. The 3-D numerical model is obtained by simply extruding the 2-D mesh along the z-axis; the in-plane (x–y) finite element mesh has therefore identical mesh refinement as the plane-strain model. Fig. 3(b) displays the 3-D finite element model for the $C(T)$ fracture specimen. Symmetry conditions enable analyses using one-quarter of the specimen with appropriate constraints imposed on the symmetry planes. The numerical model has 10 variable thickness layers defined over the half-thickness ($B/2$) with the thickest layer defined at $z = 0$. The first 8 layers lie along the crack front and the outermost 2 layers define the side groove region. The quarter-symmetric, 3-D model for this specimen has 13 026 nodes and 10 630 elements.

3.2. Finite element models for axially cracked specimens

Plane-strain finite element analyses are also conducted on longitudinally cracked pipes with varying crack configurations made of API X60 steel. The geometry and crack size match those for the pipe specimens tested in the experimental program described in Section 4 (see also Fig. 5) which included both internal and external longitudinal notches with different sizes measured by notch depth and notch length, $a \times 2c$: (1) 3×60 mm, (2) 7×140 mm and (3) 10×200 mm. Fig. 4(a) shows the finite element model constructed for the 7 mm cracked pipe specimen with internal flaw. The half-symmetric model has one thickness layer of 3497 8-node, 3-D elements with plane-strain constraints ($w = 0$) imposed on each node. Here, the finite element mesh contains a row of 88 computational cells along the remaining crack ligament ($t - a$). Similarly to the numerical model for the $C(T)$ specimens, initially squared-shaped elements are defined along the remaining crack ligament for computation of the CTOA in the pipe models. Very similar finite element models and mesh configurations are employed for other precracked pipe configurations. The numerical analyses for the pipes with internal cracks also considered crack face loading due to internal pressure.

To verify the influence of flaw length on the predicted crack growth response for the analyzed pipe specimens using the GT model, detailed 3-D finite element analyses are conducted on numerical models for the cracked pipes with both internal and external longitudinal notches. Fig. 4(b) shows the finite element model constructed for the 7 mm cracked pipe specimen with internal flaw. Very similar numerical models and mesh details are employed for the 3-D analyses of other pipe configurations.

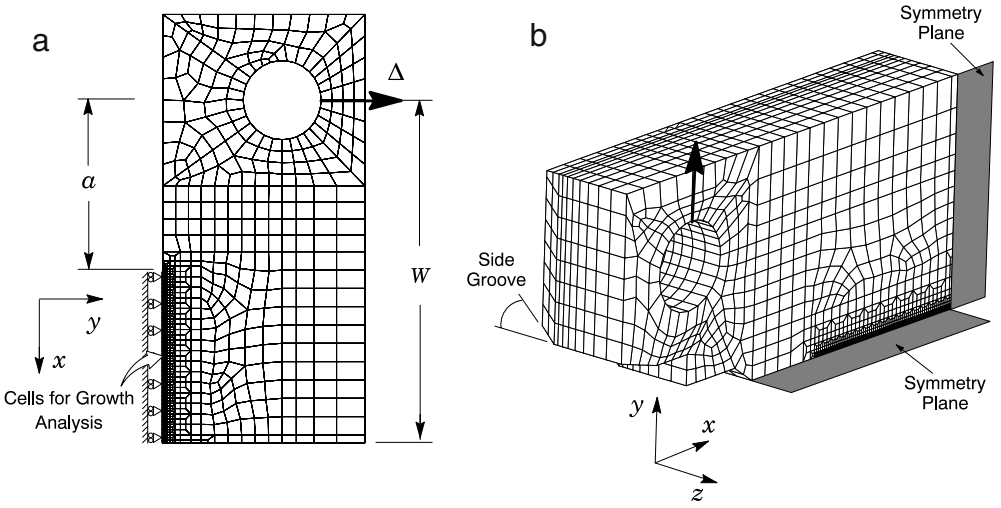

Fig. 3. Finite element models used in crack growth analyses of the deeply cracked 0.5-T $C(T)$ specimen: (a) Half-symmetric plane-strain model; (b) Quarter-symmetric 3-D model.

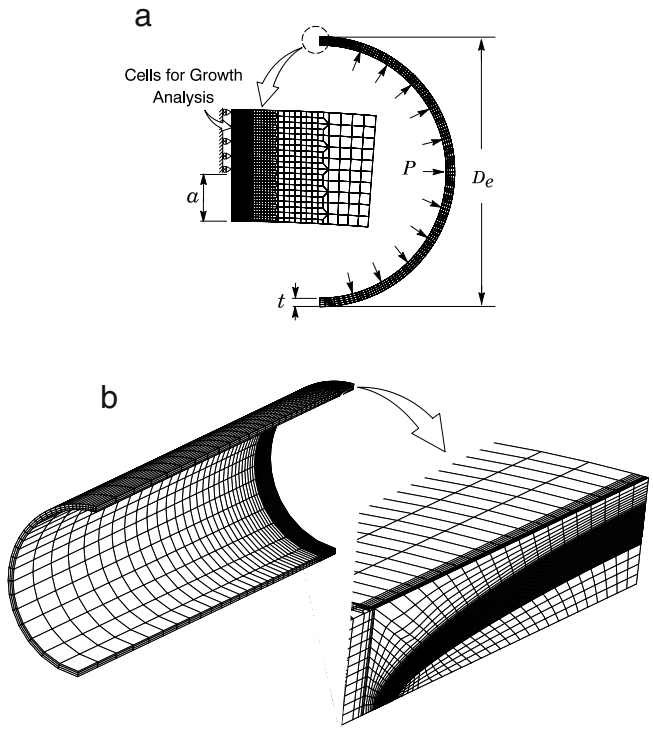

Fig. 4. Finite element models used in crack growth analyses for the pipe specimen (= eD508 mm) with 7 × 140 mm internal crack: (a) Half-symmetric plane-strain model; (b) Quarter-symmetric 3-D model.

Symmetry conditions permit modeling of only one-quarter of the specimen with appropriate constraints imposed on the symmetry planes. The quarter-symmetric model has ≈40 000 8-node, 3-D elements (≈45 000 nodes) arranged into several variable thickness layers over the half-length ($L/2$) of the specimen, as illustrated in Fig. 4(b). The crack front is described by 30 layers defined over the half-length of the crack (c); the thickest layer is defined at the deepest point of the crack with thinner layers defined near the free surface to accommodate the strong gradient in the stress distribution along the crack front. For each crack front layer, a row of 50 computational cells is arranged over the remaining crack ligament ($t - a$) thereby enabling description of ductile crack extension along the crack front.

3.3. Constitutive models and solution procedures

To describe the evolution of void growth and associated macroscopic material softening in the computational cells, the GT constitutive model given by Eq. (1) is adopted. The background material outside of the computational cells follows a flow theory with the Mises plastic potential obtained by setting $f \equiv 0$ in Eq. (1). The uniaxial true stress-logarithmic strain response for both the background and cell matrix materials follows a piecewise linear approximation to the measured tensile response for the material at room temperature described next in Section 4.

The numerical computations for the crack growth analyses reported here are generated using the research code WARP3D [38] which implements the cell model and the CTOA criterion previously described. Key features of the code also include: (1) a very efficient, sparse matrix solver highly tuned for Unix and PC based architectures to solve the equilibrium equations at each iteration, (2) the GT and Mises constitutive models implemented in a finite-strain setting, (3) automatic load step sizing based on the rate of damage accumulation, and (4) evaluation of the J-integral using a domain integral procedure [39]. WARP3D analyzes fracture models constructed with three-dimensional, 8-node trilinear hexahedral elements. To achieve plane-strain conditions for the current study, a single thickness layer of the 3-D elements is defined with out-of-plane displacements constrained to vanish. The plane-strain and 3-D analyses employ displacement control loading ($C(T)$ fracture specimen) and pressure control loading (pipe specimens) with sufficiently small load increments and a constant number of force release steps to relax forces following the cell deletion procedure.

4. Experimental program

To investigate the failure behavior of axially flawed pipelines, a series of full scale burst tests were performed on end-capped, seam welded pipe specimens with external diameter, $D_e = 508$ mm (20 in), wall thickness, $t = 15.8$ mm and length, $L = 3$ m at room temperature [41]. These experimental tests are part of a pipeline integrity program conducted by the Brazilian State Oil Company (Petrobrás). Testing of the pipe specimens included both internal and external longitudinal notches with different sizes measured by notch depth and notch length, $a \times 2c$: (1) 3×60 mm, (2) 7×140 mm and (3) 10×200 mm. To avoid any effect of the seam welding, the notches were machined at a 180° position with respect to the

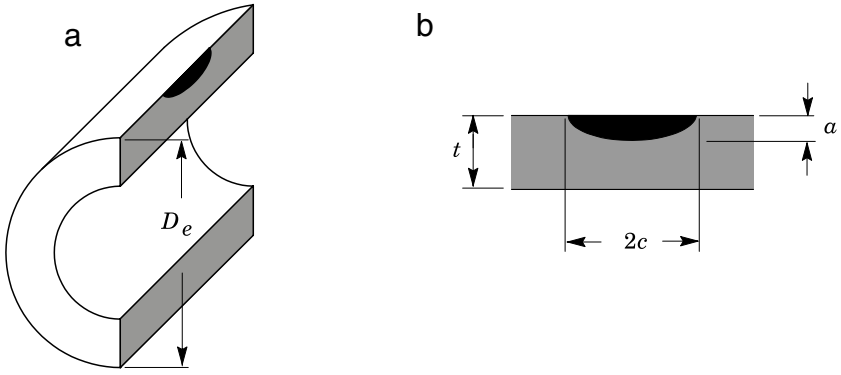

Fig. 5. Schematic illustration of the pipe specimen with external surface crack employed in the burst tests.

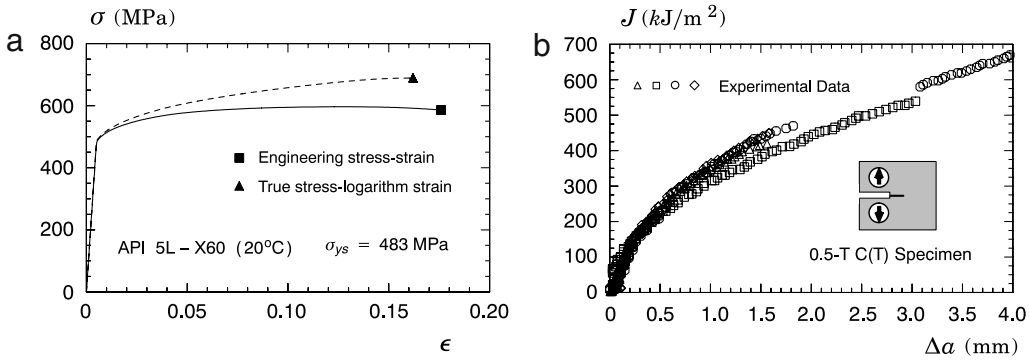

Fig. 6. (a) Uniaxial stress–strain response of API 5L X60 steel employed in the analyses [37]; (b) Experimental J-resistance curves of the tested API 5L X60 steel for the 0.5-$TC(T)$ specimens [37].

Table 1
Comparison of measured and predicted burst pressures for the pipe specimens based upon the cell model and the CTOA criterion using plane-strain analyses.

Pipe specimen $a \times 2c$ (mm)	$P_{B\text{-exp}}$ (MPa)		Cell Model $P_{B\text{-pred}}$ (MPa)		CTOA Model $P_{B\text{-pred}}$ (MPa)	
	Internal crack	External crack	Internal crack	External crack	Internal crack	External crack
3 × 60	33.0	31.5	38.3	37.6	33.2	33.1
7 × 140	27.5	25.0	27.3	26.5	20.5	20.6
10 × 200	22.0	21.0	18.8	17.6	13.4	13.9

weld. Fig. 5 schematically illustrates the tested pipes with external cracks. The pipe specimens were notched along their length using an Electrical Discharge Machine (EDM) to create the required notch shape. While the initial semi-elliptical defects were not subjected to a pressure cycle to propagate a fatigue crack from the original notch, the highly accurate machining process allows them to be considered as initially blunted cracks.

Table 1 provides the burst pressures experimentally measured in the tests, denoted P_{B-exp}; these values represent the pressure records observed immediately before the sudden drop in pressure that arises during the tests. Moreover, all tested pipe specimens exhibited abrupt collapse following intense plastic deformation of the flaw region associated with severe pipe bulging. During loading of the pipes, ductile crack extension was monitored by using an ultrasonic pulse technique to measure the crack growth at the deepest point of the surface defect [40]. These measurements revealed small amounts of ductile tearing (≈1.0 mm) prior to pipe failure. Such behavior indicates intense plastic straining directly ahead of the crack tip thereby resulting in final failure of the pipe controlled by plastic collapse rather than unstable fracture; yet, a ductile tearing analysis just prior to pipe failure is warranted.

The material is an API 5L Grade X60 pipeline steel with 483 MPa yield stress at room temperature and moderate hardening properties ($\sigma_u/\sigma_{ys} \approx 1.24$). Rectangular tensile specimens (ASTM A370) with 13 mm thickness were extracted from the circumferential orientation of the pipe (which is also the transverse direction of the steel plate) to provide the mechanical properties at room temperature [37]. Table 2 summarizes the mechanical properties obtained from these tests. Fig. 6(a) displays the engineering stress–strain data for this pipeline steel obtained using the rectangular specimens (average of three tensile tests). Here, a conventional fitting of the true stress-true strain data to the Ramberg–Osgood model [13] provides the strain hardening exponent $n = 12$ with $\alpha = 1$. Other mechanical properties for the material include Young's modulus, $E = 210$ GPa and Poisson's ratio, $\nu = 0.3$.

Laboratory testing of standard compact tension $C(T)$ specimens (side-grooved) extracted from the pipe in the TL position provided the tearing resistance curves (J vs. Δa) at room temperature (20 °C) to calibrate the cell parameters for the tested pipeline steel [37]. These fracture specimens have thickness $B = 13$ mm (0.5-T) and width $W = 26$ mm with crack length, a, to width ratio, $a/W = 0.5$ (refer to Fig. 3(a)). After fatigue pre-cracking, the specimens were side-grooved to a depth of 1 mm on each side to promote uniform crack growth over the thickness. The 0.5-T $C(T)$ specimens were tested at room temperature using a direct current potential (DCP) method to measure the crack growth resistance for the material. The fracture tests followed the procedures of ASTM Standard Test Method for Measurement of Fracture Toughness and R Curves (ASTM E1820). Experimental J-values are determined using the measured load-load line displacement records. Fig. 6(b) presents

Table 2
Mechanical properties of tested API 5L X60 steel at room temperature [37].

σ_{ys} (MPa)	σ_u (MPa)	ϵ_t (%)	σ_u/σ_{ys}
483	597	29	1.24

σ_{ys}: 0.2% proof stress; σ_u: ultimate tensile strength; ϵ_t: uniform elongation (gauge lenth = 50 mm).

the experimentally measured J vs. Δa curves; a simple extrapolation procedure indicates a value of J at initiation of ductile tearing, $J_{Ic} \approx 207$ kJ/m^2 [37]. While the experimental data for high values of ductile tearing ($\Delta a \geq 2.5$ mm) are somewhat beyond the limits given by ASTM E1820, these measured R-curves are used in a phenomenological manner (see Sections 5 and 6) in that they are essentially employed to calibrate the micromechanics parameters D and f_0 and not the toughness capacity of the fracture specimen.

5. Plane-strain analyses of ductile crack extension

The following sections provide key results of the extensive plane-strain analyses conducted on models of the $C(T)$ fracture specimen and the pipe specimens with axial flaws. The primary objective is to calibrate the micromechanics parameters using the compact tension specimen based upon the measured resistance curve and then predict the burst pressure for the pipe specimens utilizing similar analyses. While these plane-strain analyses do not fully capture the potential effects of crack front length on ductile tearing response (and, consequently, on the pipe failure pressure), they are considered sufficiently representative of the analyzed crack configurations. Subsequent sections provide further analyses on 3-D models of the $C(T)$ and pipe specimens that include effects of crack front length on the cell response.

5.1. Calibration of the GT and CTOA parameters

A key step in the procedure to predict the burst pressure in the precracked pipe specimens described next lies in the choice of the GT and CTOA parameters which govern the ductile response for the tested materials. The procedure adopted here to calibrate these parameters follows from comparison between predicted and experimentally measured fracture behavior for conventional fracture specimens such as the experimental J–Δa curve obtained from the tested deeply notched $C(T)$ specimen. Within the present context, a series of finite element analyses is conducted to calibrate the GT and CTOA parameters which establish agreement between the predicted J–Δa curve and experiments.

Consider first calibration of the cell size D and initial porosity f_0 for the GT material. While these parameters control cell response they should not be viewed as metallurgical parameters representing the microscopic observations of void spacing and initial void volume fraction but rather as computational parameters phenomenologically calibrated. Further, the calibrated values for D and f_0 clearly do not constitute a unique pair of parameters; for example, the numerical crack growth response of the fracture specimen scales almost proportionally with D for fixed f_0 (a larger cell requires more total work to reach critical conditions). However, since D introduces an explicit length scale into the model thereby requiring the construction of a new mesh, it is obviously much less effort to fix D early on and then calibrate f_0.

The approximate correlation of spacing between the large inclusions and the crack tip opening displacement (CTOD) at the onset of macroscopic crack growth in conventional fracture specimens for common pressure vessel steels provides values for D in the 50–200 μm range [21,22,26,27]. Such a range of values should also be applicable to the modeling of ductile failure behavior in a pipeline steel using the computational cells while, at the same time, providing adequate resolution of the stress–strain fields in the active layer and in the adjacent background material. Guided by previous plane-strain analyses [22,26] and experimental observations, we specify the cell size $D/2 = 100$ μm for the API X60 material employed in this study.

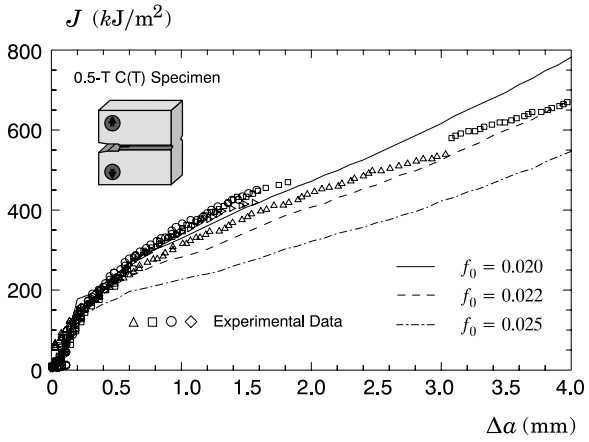

Fig. 7. Plane-strain predictions of J-resistance curves for the tested API 5L X60 steel using the computational cell model with $D/2 = 100$ μm.

With the length scale, $D/2$, fixed for the numerical analyses, the calibration process then focuses on determining a suitable value for the initial volume fraction, f_0, that produces the best fit to the measured crack growth data for the deeply cracked specimens. Dotta and Ruggieri [34] conducted a calibration procedure for this material using $q_1 = 1.43$ and $q_2 = 0.83$ taken from [25] to yield $f_0 = 0.008$ in their work. A better estimate for factors q_1 and q_2 based upon a polynomial fitting to the q-values reported by Faleskog et al. [25] provides $q_1 = 1.47$ and $q_2 = 0.94$; these values are adopted in the present analyses. Fig. 7 shows the measured (open symbols) and predicted J–Δa curves for the 0.5-$TC(T)$ specimen. Predicted R-curves are shown for three values of the initial volume fraction, $f_0 = 0.020$, 0.022 and 0.025. For consistency, the location of the growing crack tip in the analysis is taken at the cell with $f = 0.1$. As demonstrated in previous work [22,26], this corresponds to a position between the cell currently undergoing extinction and the peak stress location; at this position stresses are decreasing rapidly and the void fraction is increasing sharply. Consequently, the use of slightly different f values, other than 0.1, to define the crack tip location for plotting purposes does not appreciably alter the R-curves (at a fixed J, the amount of crack extension would vary only by a fraction of the cell size). For $f_0 = 0.020$, the predicted R-curve agrees well with the measured values for almost the entire crack extension range; for $\Delta a \geq 2$ mm the predicted curve lies a little above the measured data. In contrast, the use of $f_0 = 0.022$ and 0.025 produces a lower resistance curve relative to the measured data. Consequently, the initial volume fraction $f_0 = 0.020$ is taken as the calibrated value for the API 5L-X60 steel used in the present study.

Consider now calibration of the CTOA parameters. The key parameters characterizing the growth process which need to be specified are the initiation angle, θ_I, and the release angle, θ_R. The initiation angle controls the near-tip blunting deformation of an initially sharp crack; specification of different θ_I-values affects rather strongly the extent of the blunting region at the crack tip but has little or no influence on subsequent (stable) crack growth. The calibration procedure thus determines a suitable value for θ_I which reproduces the early stages of growth (when the crack has advanced only 4–5 cells) and then focuses on setting a release angle, θ_R, which brings the predicted J–Δa curve into agreement with the experiments over the range 1–4 mm of crack growth. Fig. 8 shows the measured (open symbols) and predicted J–Δa

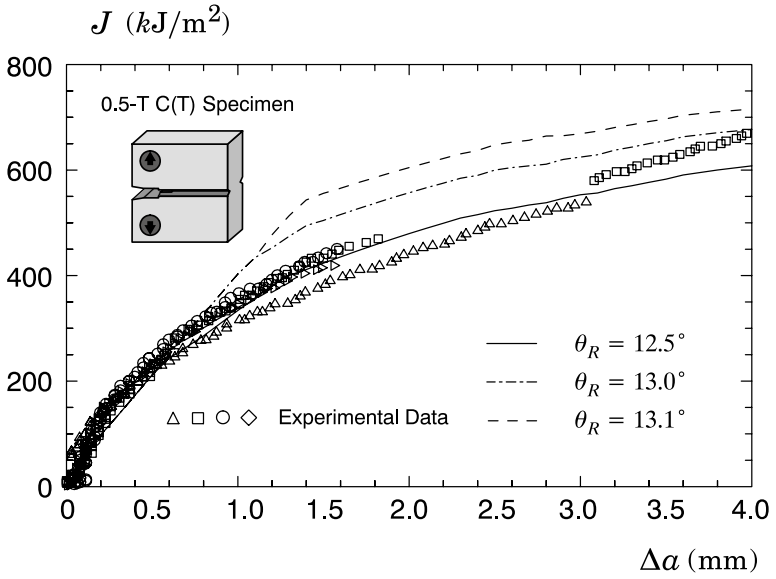

Fig. 8. Plane-strain predictions of J-resistance curves for the tested API 5L X60 steel using the CTOA model with $\theta_I = 40^\circ$.

curves for the 0.5-T $C(T)$ specimen using the CTOA model with the initiation angle adopted as $\theta_I = 40^\circ$. Predicted R-curves are shown for three values of the release angle, $\theta_R = 12.5^\circ$, 13° and 13.1°. For $\theta_R = 12.5^\circ$, the predicted R-curve agrees well with the measured values for the entire crack extension range. This value is then taken as the calibrated release angle for the API 5L-X60 steel used in the present study. In contrast, the use of $\theta_R = 13^\circ$ and 13.1° produces a higher resistance curve relative to the measured data. Here, we note the rather strong dependence of the predicted R-curve upon the value of release angle; even minor changes in the θ_R-value cause larger changes in the predicted J-value for a given amount of ductile tearing extension.

5.2. Predictions of macroscopic fracture behavior for precracked pipes

To further verify the predictive capability of the methodology adopted in the present work, this section describes a validation study to predict the measured burst pressure for the longitudinally cracked pipes based upon the cell model and the CTOA criterion. The numerical models employ plane-strain finite element analyses of these specimens using the key parameters previously calibrated: $D/2 = 100$ μm and $f_0 = 0.020$ for the cell model; $\theta_I = 40^\circ$ and $\theta_R = 12.5^\circ$ for the CTOA model. These parameters were calibrated using the 0.5-T $C(T)$ specimens and are adopted as the material-specific values in the present analyses. Moreover, the plane-strain idealization of the pipe specimen should provide a credible numerical model since the surface crack for all analyzed cases is relatively shallow and long ($a/2c = 0.05$). The next section addresses 3-D effects on pipe burst predictions.

The validation procedure of the predictive methodology presented here begins by describing ductile tearing in the precracked pipes. Fig. 9 displays the predicted evolution of crack growth with increased internal pressure for the analyzed pipe specimens using the cell model. To provide a simple comparison with the experimental data, this plot also includes the measured crack extension with increasing pressure for the pipe specimens with a 7 mm (deep crack) and 3 mm (shallow crack) internal crack which was obtained using an ultrasonic pulse technique [40]. Unfortunately, the comparisons of numerical predictions with experimental data for other pipe specimens cannot be made here as the amount of ductile tearing was monitored only for these pipe specimens. Consider first the deep crack results shown in Fig. 9. The general trend of crack growth evolution with increased

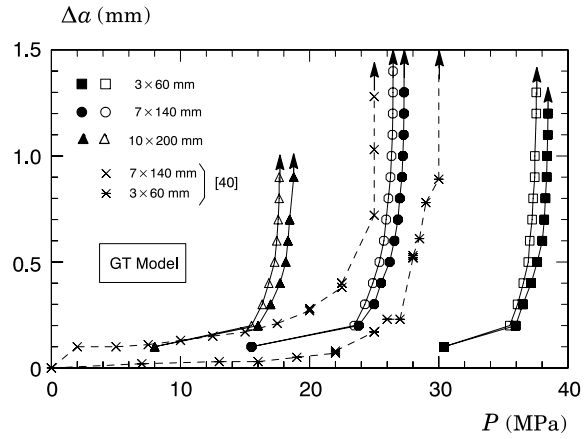

Fig. 9. Predicted evolution of crack growth for the pipe specimens using the GT model with $f_0 = 0.020$ and comparison with experimental data reported in [40] for the pipe specimens. Solid symbols represent internal cracks and open symbols represent external cracks.

pressure is correctly predicted for this pipe specimen. While the numerical predictions provide slightly higher pressure values for a fixed amount of crack growth, the analyses clearly show increased pressure values with very little crack growth just before the attainment of maximum pressure in the numerical simulations. Now consider the shallow crack results. While the overall trend of very little crack growth with increased pressure remains similar, the predicted results showed relatively poor agreement with the experimental data.

Fig. 10(a)–(d) shows the deformed profile for different load (pressure) levels, $P = 8$, 16, 24 and 27 MPa for the pipe specimen with 7 mm internal crack. The pressure value $P = 27$ MPa marks the load almost immediately prior to pipe collapse (see Fig. 9). The predicted ductile behavior reproduces the essential features of the inward deflection (bulging) mechanism in the damaged (cracked) region of the pipe as the pressure increases. Moreover, these plots aid in understanding the behavior displayed in the previous Fig. 9 where there is a rapid increase in crack growth, Δa, for small changes in the internal pressure near the attainment of the maximum pressure in the experiments. Note the substantial change in the crack opening profiles for $P = 24$ and 27 MPa in comparison with the lower pressure levels. Following a transient period

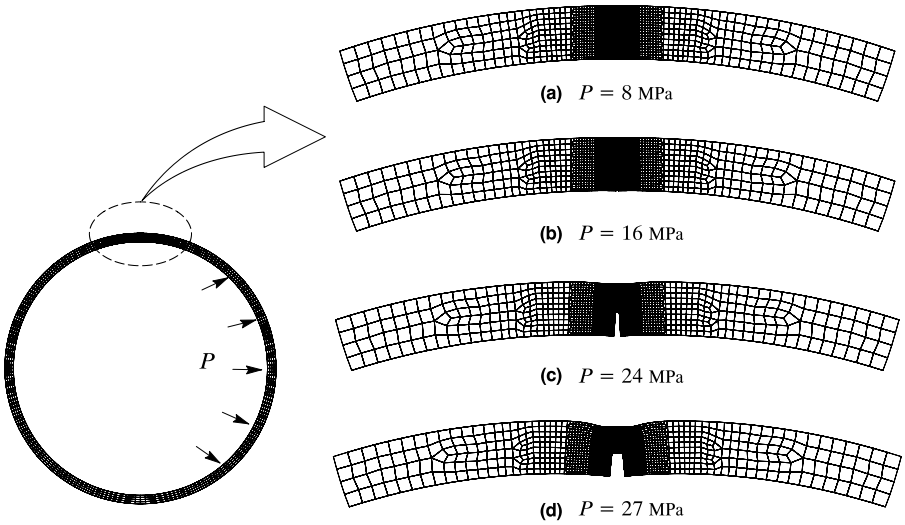

Fig. 10. Predicted evolution of bulging and crack opening for the pipe specimen with 7 × 140 mm internal crack at varying load (pressure) levels: (a) $P = 8$ MPa; (b) $P = 16$ MPa; (c) $P = 24$ MPa and (d) $P = 27$ MPa.

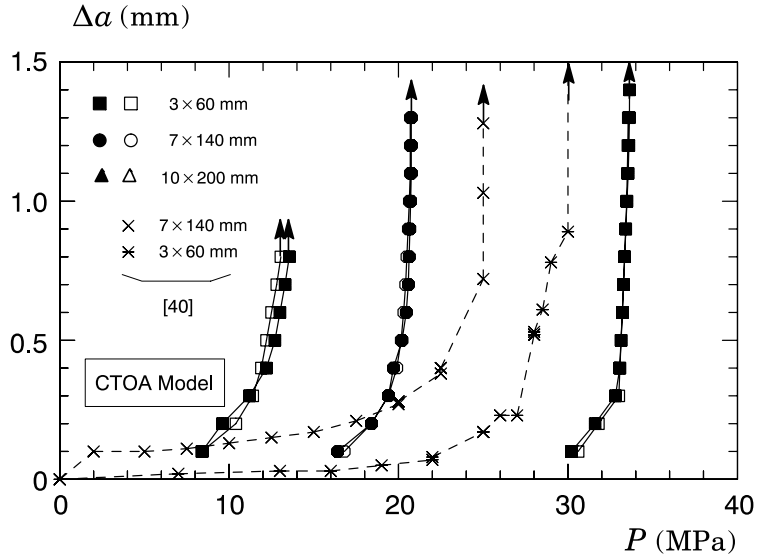

Fig. 11. Predicted evolution of crack growth for the pipe specimens using the CTOA model with $\theta_R = 12.5°$ and comparison with experimental data reported in [40] for the pipe specimens. Solid symbols represent internal cracks and open symbols represent external cracks.

when the crack mouth opening remains relatively contained, the rapid development of the inward deflection (bulging) affects rather strongly the crack mouth opening and the amount of crack extension. The numerical results reported here for the pipe specimen with the 7 mm internal crack are essentially similar to corresponding results for other pipe specimens (to conserve space, they are not shown here).

The behavior displayed by the previous results can be explained in terms of constraint effects and the (ductile fracture) process zone length, ℓ, ahead of the crack tip. Here, the fracture process zone is defined as the near-tip region encompassing the damaged cells; these cells carry only little stresses caused by material softening due to void growth. Silva et al. [42] conducted plane-strain and 3-D finite element analyses on surface cracked pipes with varying crack depth. Their analyses demonstrated that axially cracked pipelines resemble tension loaded geometries and, consequently, exhibit very low levels of crack tip constraint for all crack depths. In particular, shallow crack pipe geometries display significant loss of crack tip constraint very early in the loading. Moreover, because of the nature of the loading due to internal pressure, the membrane stress fields act over a large region of the crack ligament favoring the formation of an extended process zone $\ell/D \gg 1$ but which is nevertheless subjected to low levels of constraint and high plastic strains. Since development of the GT constitutive model (upon which the cell methodology is based) relies on high levels of stress triaxiality to drive the void growth process, crack initiation and growth behavior for the pipe specimens are strongly affected by the constraint levels ahead of the crack tip for the pipe geometries. While the cell model reproduces relatively well the evolution of crack growth with increased pressure for the deeply cracked pipe specimen, predictions for the shallow crack pipe specimen clearly show suppressed growth relative to experimental data; here, larger pressure values are necessary to activate void growth up to the levels which trigger ductile tearing in the crack ligament.

Very similar behavior is observed for the predicted evolution of crack growth with increased internal pressure using the CTOA model shown in Fig. 11. Here, the analyses also show increased pressure values with very little crack growth up to high levels of pressure followed by rapid crack extension just before final failure. However, while the agreement between numerical predictions and experiments is improved for the shallow cracked pipe (albeit

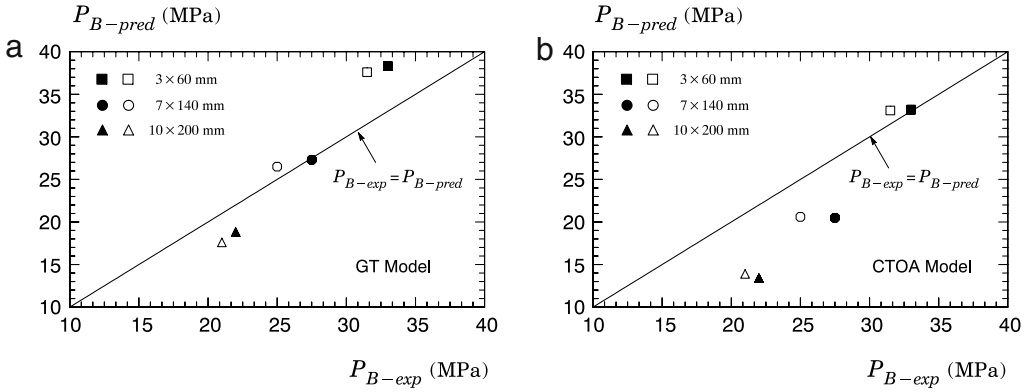

Fig. 12. Predicted burst pressures for the tested pipe specimens: (a) GT model; (b) CTOA model. Solid symbols represent internal cracks and open symbols represent external cracks.

still providing differences of ∼20%), larger deviations now arise between predictions and experiments for the deeply cracked pipe. These features are consistent with observations about the very low levels of crack tip constraint coupled with the strong membrane loading acting on the crack ligament made previously.

The results displayed in Figs. 9 and 11 serve to introduce a simple criterion which defines the failure pressure for the analyzed pipe specimens. Under increased internal pressure, the amount of crack growth increases slowly up to pressure values which are close to the attainment of the maximum pressure in the analyzes. After this pressure level, the region of damaged material ahead of the crack tip increases very rapidly thereby causing a significant crack extension just before final failure. When an instability point is eventually reached (points marked by arrows in Figs. 9 and 11), the remaining material in the crack ligament defined by $t - a$ (see Fig. 5) cannot keep pace with the increased pressure so that pipe collapse occurs.

Fig. 12 provides the predicted burst pressure for the tested pipes using both crack growth models. The symbols in the plots represent the predicted values whereas the solid line defines equality between the experiments and predictions, i.e., $P_{B\text{-exp}} = P_{B\text{-pred}}$; here, the solid symbols define predicted values for the internal cracks and the open symbols correspond to the external cracks. Table 1 compares the predicted burst pressures with the experimentally measured values. Consistent with the results already displayed in Figs. 9 and 11, the cell model provides good agreement between predicted values and experiments for the deeply cracked pipes and largely overestimates the experimental pressure values for the shallow crack pipes. These results contrast sharply with the predictions derived from the CTOA model; much lower pressure values are predicted for the deep crack pipes whereas the predictions slightly overestimate the experimental pressure values for the shallow cracked pipes.

6. 3-D effects on the cell model response for cracked pipelines

The previous plane-strain analyses of the pipe specimens provided a means to describe the thickness average features of macroscopic fracture behavior in cracked pipelines while, at the same time, giving valuable insight into the overall response of the cell methodology. In this section, we address 3-D effects on the cell model response for the analyzed crack configurations to include the influence of crack front length on the predicted failure pressure. Because of the rather overall poor agreement between experiments and predictions derived from the CTOA criterion, the present analyses focus on 3-D computations describing crack extension in the pipe specimen based upon the GT model.

6.1. Calibration of the GT parameters

Calibration of the cell parameters, D and f_0, based upon 3-D analyses of the 0.5-T $C(T)$ specimens follows essentially the same procedures outlined previously. The cell size is assigned the same value corresponding to the plane-strain analyses, $D/2 = 100$ μm, while the initial volume fraction, f_0, is calibrated to establish agreement between predicted and measured R-curves. In the analyses described here, factors q_1 and q_2 for the tested pipeline steel are also adopted as $q_1 = 1.47$ and $q_2 = 0.74$ as given previously in Section 5.1.

Fig. 13 shows the predicted, 3-D J-resistance curves for the $C(T)$ fracture specimen computed using three values for the initial volume fraction, $f_0 = 0.011$, 0.015 and 0.020. The lines in the plot represent a mean resistance curve obtained by a weighted average taken over the half-thickness for the various f_0-values whereas the open symbols indicate each of the four measured R-curves with crack extensions estimated using DCP data. While the general behavior displayed by this plot is similar to the plane-strain analyses, the f_0-value which brings the predicted R-curve in agreement with the measured data is lower. This can be understood in terms of differences in crack tip constraint between the plane-strain and 3-D models. Previous work by Silva et al. [42] using detailed 3-D models of fracture specimens reveals that constraint over the crack front differs significantly from the levels given by plane-strain analyses of deep notch $C(T)$ specimens. As a consequence of load redistribution over the 3-D crack front, a high level of stress triaxiality at the centerplane persists to larger J-values than indicated in plane-strain models. This maintenance of high stress triaxiality in the 3-D model coupled with the plane-strain initial porosity, $f_0 = 0.020$, would lead to a larger amount of crack growth at the centerplane of the specimen. Consequently, the lower volume fraction, $f_0 = 0.011$, taken here as the calibrated 3-D value, offsets the increase in crack tip constraint.

6.2. 3-D effects on failure pressure predictions of axially cracked pipes

To verify the effectiveness of the current cell model in failure pressure predictions for the tested pipe specimens, the 3-D pipe models are analyzed with the cell parameters set to the previous calibrated values of $D/2 = 100$ μm and $f_0 = 0.011$. The analyses proceed in a similar manner as outlined before for the plane-strain models. Under increased internal pressure, the amount of crack growth increases slowly up to pressure values close to the attainment of the maximum pressure in the analyzes. After this pressure level, the region of damaged material ahead of the crack tip increases very rapidly thereby reaching an instability point which marks the failure pressure for the pipe.

Table 3
Comparison of measured and predicted burst pressures for the pipe specimens based upon the cell model using 3-D analyses. Predictions from BS7910 procedure are also included.

Pipe specimen $a \times 2c$ (mm)	$P_{B\text{-exp}}$ (MPa)		Cell model $P_{B\text{-pred}}$ (MPa)		BS7910 L2A $P_{B\text{-pred}}$ (MPa)
	Internal crack	External crack	Internal crack	External crack	Internal/external crack
3 × 60	33.0	31.5	35.3	36.6	21.4
7 × 140	27.5	25.0	28.0	25.8	19.3
10 × 200	22.0	21.0	20.3	19.3	14.2

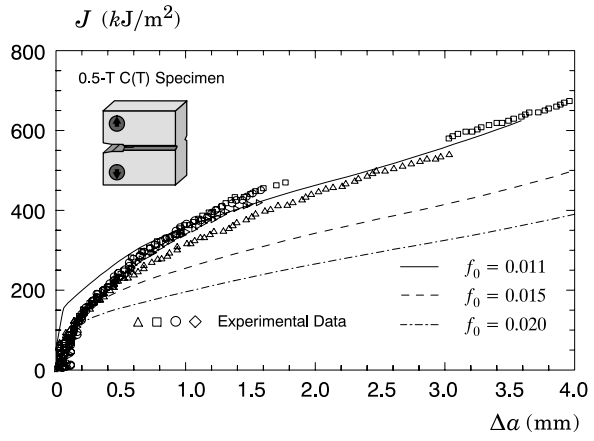

Fig. 13. Predicted J-resistance curves of the tested API 5L X60 steel for the 0.5-T $C(T)$ specimens in 3-D using the computational cell model with $D/2 = 100\ \mu$m.

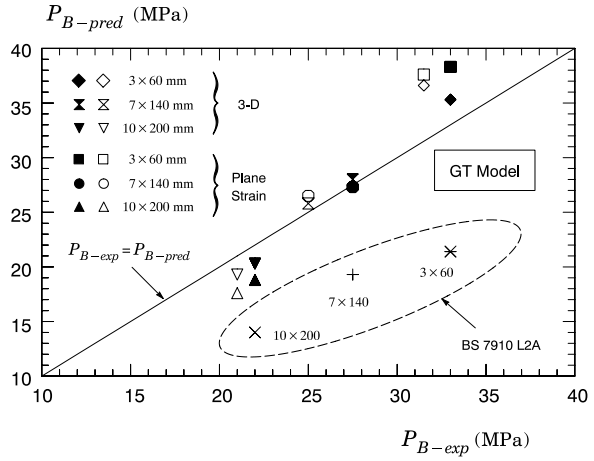

Fig. 14. Predicted burst pressures for the tested pipe specimens in 3-D using the GT model.

Fig. 14 provides the predicted burst pressure for the tested pipes derived from the cell methodology incorporating the GT model using the 3-D analyses. The symbols in the plots represent the predicted values whereas the solid line defines equality between the experiments and predictions, i.e., $P_{B\text{-exp}} = P_{B\text{-pred}}$; here, the solid symbols define predicted values for the internal cracks and the open symbols correspond to the external cracks. To facilitate comparisons, the predicted values from the plane-strain analyses are also provided in the plot. Additional analyses using a simplified engineering approach for defect assessments based upon the BS 7910 procedure [9] were also conducted and enable further comparisons with the experimental values for the tested pipes; these predicted burst pressures are also included in the plot. The Annex provides an overview of the two-criteria failure assessment diagram methodology upon which BS 7910 is derived.

Predictions for the tested pipes based upon the 3-D analyses show slightly better agreement with the experimental values. Table 3 provides the predicted burst pressures in 3-D with

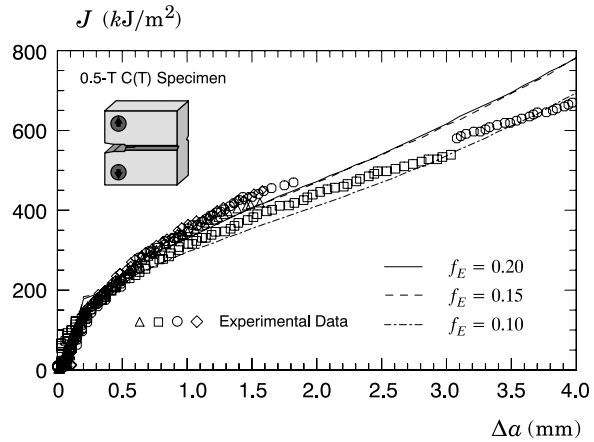

Fig. 15. Effect of critical porosity, f_E, on predicted J-resistance curves of the tested API 5L X60 steel using the cell model with $f_0 = 0.02$.

the experimentally measured values; predictions from the BS 7910 procedure [9] are also included. However, the trends displayed by these 3-D results are essentially similar to the plane-strain analyses (see also Section 5.2). As already observed, the cell model provides good agreement between predicted values and experiments for the deeply cracked pipes and largely overestimates the experimental pressure values for the shallow crack pipes. Even using the refined and detailed 3-D models of these crack configurations, the failure to predict the experimental burst pressure more accurately for the shallow crack pipes still persists. In contrast, the analyses using BS 7910 predict much lower failure pressures for all cracked pipe configurations indicating a large overconservatism in failure pressure estimations based upon this methodology.

7. Further numerical aspects

Previous work [27,31] and our own numerical experience have shown that computational issues often affect analyses employing the cell model and the CTOA criterion to predict crack growth resistance curves for common fracture specimens. These issues raise concerns about the applicability and robustness of these methodologies in defect assessments of thin-walled pipelines. Valuable insight into the relation between macroscopic fracture behavior and the predicted pressure values for the tested pipe specimens can be gained by examining the significance of some numerical details. Here, attention is directed to effects of key parameters on the ductile tearing response which have a direct bearing on the predicted pressure values for the tested pipe specimens. Specifically, the following sections address the effects of the number of force release steps on macroscopic fracture response for the analyzed specimens using both methodologies. Further, the effect of critical porosity, f_E, on predictions of crack growth response derived from the cell model is also examined.

7.1. Effects of f_E and force release on cell model response

Specification of the critical porosity, f_E, required in applications of the cell methodology controls the activation of the element

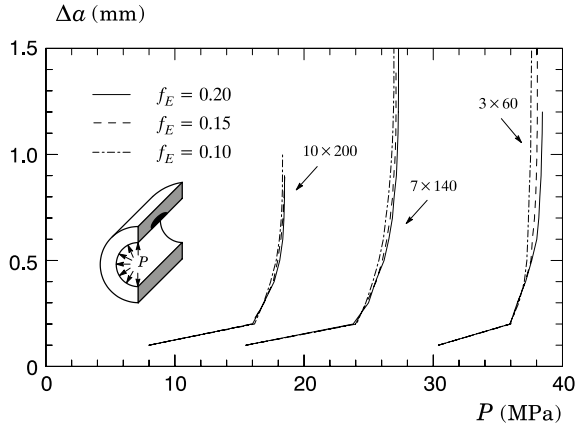

Fig. 16. Effect of critical porosity, f_E, on predicted evolution of crack growth for the pipe specimens with internal cracks using the cell model with $f_0 = 0.02$.

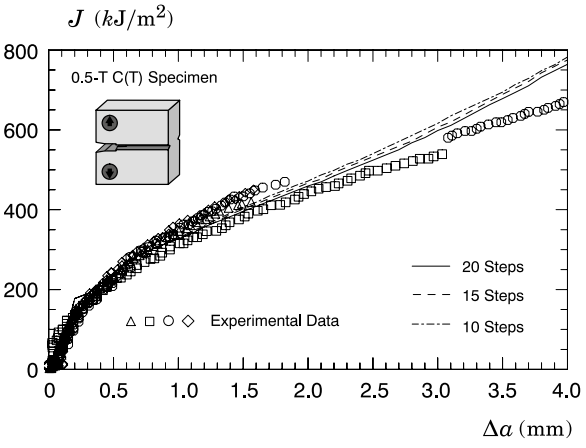

Fig. 17. Effect of number of force release steps on predicted J-resistance curves of the tested API 5L X60 steel using the cell model with $f_0 = 0.02$.

extinction procedure outlined previously. Following the attainment of a peak macroscopic stress, the cell (macroscopic) stresses drop sharply at $f = f_E$ with further cell deformation producing an approximately linear decay of stress to zero. While the use of different f_E-values affects the cell deletion procedure (and, consequently, the predicted macroscopic growth behavior), there should be an adequate range of f_E-values over which the predicted pressure values for the pipe specimens display minor sensitivity.

Fig. 15 displays the predicted R-curve for the 0.5-T $C(T)$ specimen using the cell model with $f_0 = 0.020$ for varying values of critical porosity, $f_E = 0.10$, 0.15 and 0.20; these values are within the range of critical void fractions commonly employed in numerical analyses. The numerical resistance curves derived from the analyses with the adopted f_E-values provide similar response, particularly for $f_E = 0.15$ and 0.20. Here, we note that using $f_E = 0.10$ yields a lower resistance curve since deletion of the cells occurs at lower levels of loading (as measured by J). Fig. 16 shows the macroscopic crack growth behavior for the analyzed pipe specimens with $f_0 = 0.020$ and $f_E = 0.10$, 0.15 and 0.20. For each cracked pipe geometry, the P–Δa curves are essentially similar and display a very minor sensitivity to the critical porosity value.

Similar behavior arises from examining the effect of the number of force release steps, N_{rs}, on macroscopic fracture response for the analyzed crack configurations. Figs. 17 and 18 show the predicted R-curve for the 0.5-T $C(T)$ specimen and the cracked pipes using $f_0 = 0.020$ with $N_{rs} = 10$, 15 and 20 steps. The trends are clear and consistent with the role played by f_E in relation to the cell deletion procedure displayed previously. For all analyzed crack configurations, the results shown in those plots clearly reveal that ductile tearing response is essentially independent of N_{rs}.

The very low sensitivity of macroscopic crack growth on the force release process and the critical porosity resulting from the previous analyses is potentially connected to the effect of the load step size on the computed resistance curves. For fixed values of N_{rs} (and to a lesser extent, f_E), larger load increments alter the cell deletion procedure and the relaxing of nodal forces after an element has been extinguished. Gullerud et al. [27] discuss this issue in detail and provide further results which support the significance of the load step size in numerical predictions of ductile tearing within the present methodology. However, as emphasized previously, the analyses conducted here utilize sufficiently small load increment sizes over the entire prescribed loading coupled with an adaptive load control algorithm [38]; such a strategy enables rapid convergence of the iterative procedure in the finite element solutions. While these computational issues may play a central role in large-scale 3D analyses where the computational demands are much higher, we consider the present results (which

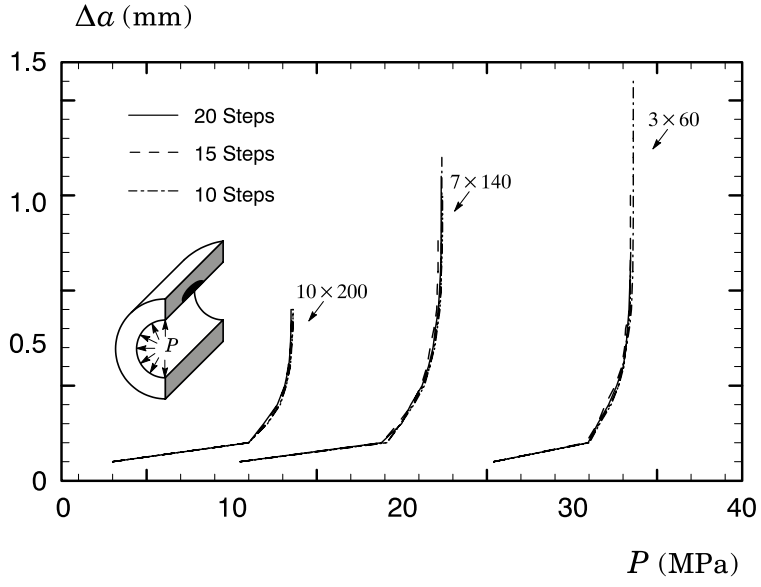

Fig. 18. Effect of number of release steps on predicted evolution of crack growth for the pipe specimens with internal cracks using the cell model with $f_0 = 0.02$.

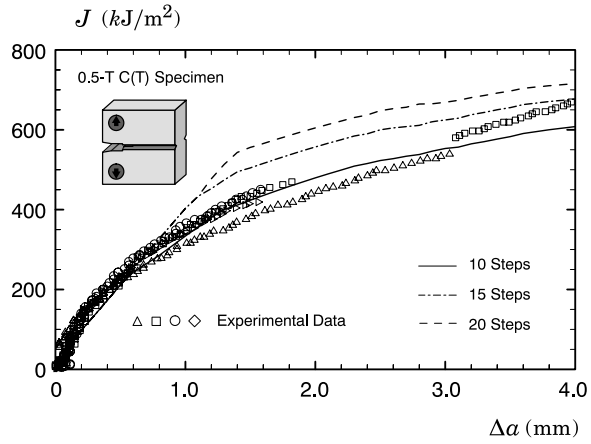

Fig. 19. Effect of number of force release steps on predicted J-resistance curves of the tested API 5L X60 steel using the CTOA model with $\theta_R = 12.5^\circ$.

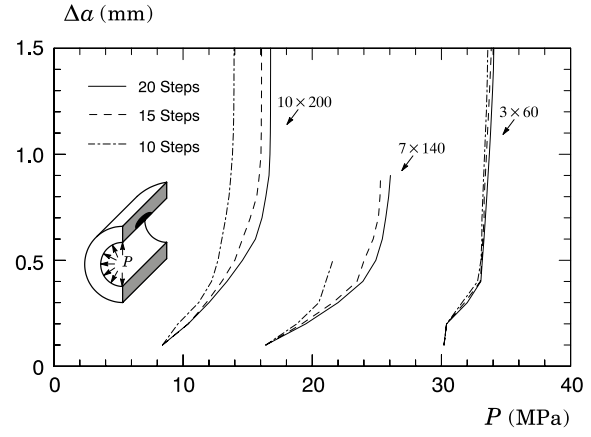

Fig. 20. Effect of number of force release steps on predicted evolution of crack growth for the pipe specimens with internal cracks using the CTOA model with $\theta_R = 12.5^\circ$.

are based upon plane-strain analyses) suffice to demonstrate the effectiveness of the cell methodology in describing the crack growth response for thin-walled pipelines with planar cracks.

7.2. Effects of force release on CTOA predictions

Fig. 19 displays the predicted R-curve for the 0.5-T $C(T)$ specimen using the CTOA model with $\theta_R = 12.5^\circ$ for different force release steps, $N_{rs} = 10$, 15 and 20. In contrast to the previous analyses using the cell model, the adopted N_{rs} displays greater effect on macroscopic growth response for this fracture specimen, particularly within the range of 10–15 release steps. Similar observations follow from analyzing the effect of N_{rs} upon the tearing resistance for the cracked pipes shown in Fig. 20. However, the evolution of P with Δa is much less sensitive for the shallow cracked pipe than for the other cracked geometries.

The more prominent role played by the number of force release steps in defining the macroscopic fracture response for the analyzed cracked configurations using the CTOA model can be explained in terms of the nodal release procedure coupled with the growth controlling mechanism. Consider first the resistance curve for the fracture specimen derived from using $N_{rs} = 10$ steps displayed in Fig. 19. This curve provides an adequate description of the evolution of J versus Δa for the entire range of ductile crack growth; here, the release process has plausibly a minor effect on subsequent crack tip deformation thereby not affecting the

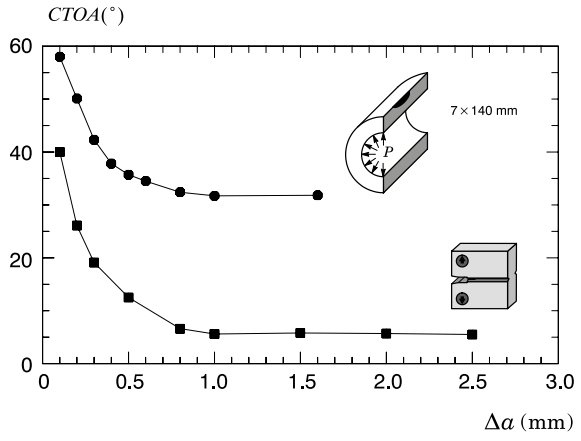

Fig. 21. Evolution of CTOA with crack extension for the deeply cracked 0.5-T $C(T)$ specimen and the 7 × 140 mm precracked pipe specimen derived from the cell model.

(constant) CTOA for crack growth. In contrast, when $N_{rs} = 20$ steps, the remaining forces in released nodes resist further opening of the crack caused by increased deformation with a potential for "artificially" holding the crack closed. Consequently, the release process has a great effect on the CTOA for crack growth; here, for a given amount of ductile tearing, larger values of J and pressure P are required to reach the specified CTOA for crack advancement.

7.3. Dependence of CTOA on component geometry

Application of the CTOA concept as a growth criterion in cracked structural components assumes independence of the CTOA during stable crack growth, on specimen geometry. A number of previous studies [28–33] consistently reveal a weak dependence of the critical CTOA on specimen size for thin panels and fracture specimens while others show a relatively more pronounced dependence of θ_R on thicker specimen geometries. The relatively limited analyses available to describe crack growth resistance behavior for axially cracked pipelines based upon the CTOA underscores the need for further investigation.

Fig. 21 shows the computed CTOA derived from plane-strain analyses conducted for the deeply cracked, 0.5-T $C(T)$ fracture specimen and the pipe specimen with an external crack of 7 × 140 mm. The CTOA is directly computed from the deformation of the nodes at the crack tip derived from analyses using the cell model. After a transient stage of ductile tearing, $\Delta a \approx 0.5$ mm (where crack growth is driven by a nonconstant CTOA value), crack extension for both configurations continues under a nearly constant CTOA value. However, the strong dependence of CTOA during stable crack growth on specimen geometry is evident. Clearly, such behavior is associated with the dominant loading conditions in both crack configurations. The $C(T)$ specimen is primarily a bend configuration whereas the cracked pipe under internal pressure is primarily subjected to strong membrane loading. Consequently, the assumption of a constant CTOA value calibrated from using the $C(T)$ fracture specimen accentuates the relatively poor agreement between measured and predicted burst pressures which is precisely the result shown in Figs. 11 and 12.

8. Concluding remarks

This study described a micromechanics approach based upon the computational cell methodology incorporating the Gurson–Tvergaard model and a deformation-based approach using the

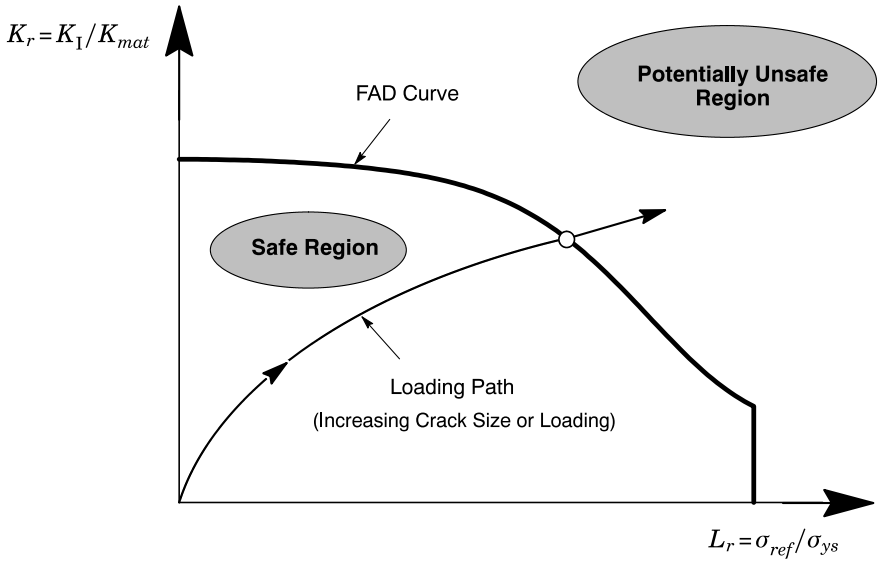

Fig. A.1. Schematic illustration of the FAD methodology.

CTOA criterion to predict experimentally measured burst pressures for thin-walled gas pipeline containing longitudinal cracks. The numerical simulations demonstrate the effectiveness and limitations of both approaches to describe crack growth response and to predict the burst pressure for the tested pipes. The verification study shows the potential predictive capability of the cell approach incorporating the GT model, particularly for moderate to deep crack size to pipe thickness ratios (a/t); however, burst pressure predictions for the shallow crack pipe specimen displayed poor agreement with experiments and largely overestimated the measured failure pressures. In contrast, the CTOA criterion provided rather overall poor agreement between experiments and predictions. Further, the plane-strain analyses demonstrated a strong dependence of CTOA during stable crack growth on crack configuration thereby imposing additional difficulties in adopting this parameter as a viable criterion for burst pressure predictions in high pressure pipes. Nevertheless, the results presented here lend additional support for further developments in the cell methodology as an engineering tool for integrity assessments of pipelines with axial defects. Further experimental and computational studies are in progress to assess the failure behavior of axially cracked pipes made of an X70 grade steel. This work also involves testing of single edge notch tension specimens (SE(T) geometry) to measure the ductile tearing properties for calibration of the cell parameters.

Acknowledgements

This investigation is supported by the Brazilian Council for Scientific and Technological Development (CNPq) through Grant 304132/2009-8. The authors acknowledge the Brazilian State Oil Company (Petrobrás) for making available the X60 pipeline steel data and the burst pressure data.

Appendix. Overview of the FAD methodology

It is widely recognized that brittle fracture and plastic collapse caused by overloading are competing failure modes in cracked structural components made of materials with sufficient toughness. Early work by Dowling and Townley [43] and Harrison et al. [44] to address the potential interaction between fracture and plastic collapse introduced the concept of a two-criteria failure assessment diagram (most often referred to as FAD) to describe the mechanical integrity of flawed components as schematically illustrated in Fig. A.1.

In the FAD methodology, a roughly geometry and material independent failure line is constructed based upon a relationship between the normalized crack tip loading, K_r, and the normalized applied (remote) loading, L_r, in the form

$$K_r = f(L_r), \tag{A.1}$$

where

$$K_r = \frac{K_I(P, a)}{K_{\text{mat}}}, \tag{A.2}$$

and

$$L_r = \frac{P}{P_L(a, \sigma_{ys})}. \tag{A.3}$$

Here P is the applied (remote) load, K_I is the elastic stress intensity factor, K_{mat} is the material's fracture toughness, σ_{ys} is the yield stress and P_L is the value of P corresponding to plastic collapse of the cracked component. Alternatively, parameter L_r can be defined in terms of a reference stress, σ_{ref}, defining the plastic collapse load solution of the remaining crack ligament as

$$L_r = \frac{\sigma_{\text{ref}}}{\sigma_{ys}}. \tag{A.4}$$

Current defect assessment procedures based on Eq. (A.1) include the BS7910 [9] and API 579 [10]. Both methodologies have emerged as engineering codes widely used for defect assessments which incorporate a three-tiered (or three-level) FAD criterion with increasing analytical sophistication and data requirements and decreasing conservatism. The normal crack-flaw assessment in BS7910 is Level 2A and in API 579 is Level 2 which utilize the following FAD expression

$$K_r = \lfloor 1 - 0.14(L_r)^2 \rfloor \{0.3 + 0.7 \exp\lfloor -0.65(L_r)^6 \rfloor\}, \quad L_r \le L_r^{\max}, \tag{A.5}$$

where the cut-off parameter, $L_r^{\max}$, is most often defined in terms of the flow stress, $\sigma_f = (\sigma_u + \sigma_{ys})/2$, in the form

$$L_r^{\max} = \frac{1}{2}\left(\frac{\sigma_u + \sigma_{ys}}{\sigma_{ys}}\right), \tag{A.6}$$

where σ_u denotes the material's tensile strength. The cut-off parameter defined by Eq. (A.6) reflects a simplified criterion to prevent localized plastic collapse while, at the same time, taking account of the hardening effect above yielding observed in ferritic carbon steels and austenitic stainless steels.

Structural integrity assessments of a cracked component are based on the relative location of the assessment point with respect to the FAD curve defined by Eq. (A.5) (see Fig. A.1). The component is simply considered safe if the assessment point lies below the FAD line whereas it is considered potentially unsafe if the assessment point lies on or above the FAD curve. An increased load or larger crack will move the assessment point along the loading path towards the failure line.

Key steps to determine (K_r, L_r) at failure based upon BS 7910 [9] include evaluation of the stress intensity factor and reference stress based upon the primary load. Following Annex M of BS 7910, the stress intensity factor solution employed in the present study is given by

$$K_I = Y\sigma_0\sqrt{\pi a}, \tag{A.7}$$

where a is the crack depth, σ_0 is the applied primary stress (due to membrane loading on the crack faces) and factor Y is defined as

$$Y = Mf_w M_m, \tag{A.8}$$

where M is the bulging correction factor (which is also known as the Folias factor for thin-walled cylinders [45]), M_m is the stress magnification factor and f_w is the finite width correction. Annex M of BS7910 provides analytical expressions for parameters M, M_m and f_w as a function of a/t and c/a.

Now, following Annex P of BS7910, the reference stress, σ_{ref}, for a surface flaw oriented axially in a cylinder is given by

$$\sigma_{\text{ref}} = 1.2M_s\sigma_0, \tag{A.9}$$

where M_s is again the Folias bulging factor defined as

$$M_s = \frac{1 - [a/(tM_T)]}{1 - (a/t)}, \tag{A.10}$$

with parameter M_T expressed by

$$M_T = \sqrt{1 + 1.6\left(\frac{c^2}{R_i t}\right)}, \tag{A.11}$$

where R_i is the internal radius of the pipe.

References

[1] Eiber RJ, Kiefner JF. Failure of pipelines. In: Metals handbook. ninth ed. Failure analysis and prevention, vol. 11. American Society for Metals; 1986. p. 695–706.
[2] American Welding Society. Welding handbook: welding technology. Eighth edition. Miami. vol. 1. 1987.
[3] National Energy Board. Stress corrosion cracking on Canadian oil and gas pipelines. Report MH-2-95. Calgary. 1996.
[4] The American Society of Mechanical Engineers. Manual for determining the remaining strength of corroded pipelines. ASME B31-G. New York. 1984.
[5] Kiefner JF, Maxey WA, Eiber RJ, Duffy AR. Failure stress levels of flaws in pressurized cylinders. In: Progress in flaw growth and fracture toughness testing. ASTM STP, 536. Philadelphia: American Society for Testing and Materials; 1973. p. 461–81.
[6] The American Society of Mechanical Engineers. Boiler and pressure vessel code—section XI. 2004.
[7] Wilkowski G, Stephens G, Krishnaswamy P, Leis B, Rudland D. Progress in development of acceptance criteria for local thinned areas in pipe and piping components. Nucl Eng Des 2000;149–69.
[8] British Energy. Assessment of the integrity of structures containing defects. R6 revision 4. 2003.
[9] British Standard Institution. Guide on methods for assessing the acceptability of flaws in metallic structures. BS7910. 1999.
[10] American Petroleum Institute. Recommended practice for fitness-for-service. API RP-579. 2000.
[11] SINTAP: structural integrity assessment procedure for European industry. Final procedure. 1999.
[12] Hutchinson JW. Fundamentals of the phenomenological theory of nonlinear fracture mechanics. J Appl Mech 1983;1042–51.
[13] Anderson TL. Fracture mechanics: fundaments and applications. 3rd ed. New York: CRC Press; 2005.
[14] Joyce JA, Hackett EM, Roe C. Effects of crack depth and mode loading on the J–R curve behavior of a high strength steel. In: Hackett EM, et al., editors. Constraint effects in fracture. ASTM STP, 1171. Philadelphia: American Society for Testing and Materials; 1993. p. 239–63.
[15] Joyce JA, Link RE. Effects of constraint on upper shelf fracture toughness. In: Reuter WG, et al., editors. Fracture mechanics. ASTM STP 1256, vol. 26. Philadelphia: American Society for Testing and Materials; 1995. p. 142–77.
[16] Pineau A. Global and local approaches to fracture-transferability of laboratory test data to components. In: Argon AS, editor. Topics in fracture and fatigue. Springer Verlag; 1992. p. 197–234.
[17] Bilby BA, Howard IC, Li ZH. Some experience in the use of damage mechanics to simulate crack behavior in specimens and structures. Int J Press Vessels Pip 1995;64:213–23.
[18] Brocks W, Klingbeil D, Kuenecke G, Sun D-Z. Applications of the Gurson model to ductile tearing. In: Kirk MT, Bakker A, editors. Constraint effects in fracture, theory and applications. ASTM STP, 1244. Philadelphia: American Society for Testing and Materials; 1995.
[19] Burstow MC, Howard IC. Predicting the effects of crack tip constraint on material resistance curves using ductile damage theory. Fatigue Fract Eng Mater Struct 1996;19(4).
[20] Li ZH, Howard IC, Bilby BA. Three-dimensional damage theory of crack growth in large center cracked panels using the element removal technique. Nucl Eng Des. 1997;172:1–12.
[21] Xia L, Shih CF. Ductile crack growth—I. A numerical study using computational cells with microstructurally-based length scales. J Mech Phys Solids 1995;43:233–59.
[22] Xia L, Shih CF. Ductile crack growth—II. Void nucleation and geometry effects on macroscopic fracture behavior. J Mech Phys Solids 1995;43:1953–81.
[23] Gurson AL. Continuum theory of ductile rupture by void nucleation and growth: part I—yield criteria and flow rules for porous ductile media. J Eng Mater Technol 1977;99:2–15.
[24] Tvergaard V. Material failure by void growth to coalescence. Advances in Applied Mechanics 1990;27:83–151.
[25] Faleskog J, Shih CF. Cell model for nonlinear fracture analysis—I: micromechanics calibration. Int J Fract 1998;89:355–73.
[26] Ruggieri C, Panontin TL, Dodds RH. Numerical modeling of ductile crack growth in 3-D using computational cells. Int J Fract 1996;82:67–95.
[27] Gullerud AS, Gao X, Dodds RH, Haj-Ali R. Simulation of ductile crack growth using computational cells: numerical aspects. Eng Fract Mech 2000;66:65–92.
[28] Shih CF, de Lorenzi HG, Andrews WR. Studies on crack initiation and stable crack growth. In: Landes JD, et al., editors. Elastic–plastic fracture. ASTM STP, 668. Philadelphia: American Society for Testing and Materials; 1979. p. 65–120.
[29] Newman Jr JC. An elastic–plastic finite element analysis of crack initiation stable crack growth and instability. In: Stanford RJ, editor. Fracture mechanics. ASTM STP, 833. Philadelphia: American Society for Testing and Materials; 1984. p. 93–117.
[30] Newman Jr JC, Booth BC, Shivakumar KN. An elastic–plastic finite element analysis of the J-resistance curve using a CTOD criterion. In: Stanford RJ, editor. Fracture mechanics. ASTM STP, 945. Philadelphia: American Society for Testing and Materials; 1988. p. 665–85.
[31] Gullerud AS, Dodds RH, Hampton RW, Dawicke DS. Three-Dimensional modeling of ductile crack growth in thin sheet metals: computational aspects and validation. Eng Fract Mech 1999;63:347–74.
[32] Deng X, Newman Jr JC. A study of some issues in stable tearing crack growth simulations. Eng Fract Mech 1999;64:291–304.
[33] Newman Jr JC, James MA, Zerbst U. A review of the CTOA/CTOD criterion. Eng Fract Mech 2003;70:371–85.
[34] Dotta F, Ruggieri C. Structural integrity assessment of high pressure pipelines with axial flaws using a micromechanics model. Int J Press Vessels Pip 2004;81:761–70.
[35] Garrison Jr WM, Moody NR. Ductile fracture. J Phys Chem Solids 1987;48:1035–74.
[36] Zhang ZL, Thaulow C, Ødegård J. A complete Gurson model approach for ductile fracture. Eng Fract Mech 2000;67:155–68.
[37] Silva MS. Fracture toughness and R-curve measurements for an API X60 pipeline steel using a direct current potential technique. M.Sc. thesis. Faculty of Engineering. COPPE. Federal University of Rio de Janeiro. 2002 [in Portuguese].
[38] Gullerud A, Koppenhoefer K, Roy A, RoyChowdhury S, Walters M, Bichon B, Cochran K, Dodds R. WARP3D: dynamic nonlinear fracture analysis of solids using a parallel computers and workstations. Structural research series (SRS) 607. UILU-ENG-95-2012. University of Illinois at Urbana-Champaign. 2004.
[39] Moran B, Shih CF. A General treatment of crack tip contour integrals. Int J Fract 1987;35:295–310.
[40] Petrobras. Ultrasonic measurements in burst pressure tests for a 20 O.D. API grade 5L X60 pipelines. Private report. 2002 [in Portuguese].
[41] Petrobras. Burst pressure tests in 20 O.D. API grade 5L X60 pipelines. Private report. 2002 [in Portuguese].

[42] Silva LAL, Cravero S, Ruggieri C. Correlation of fracture behavior in high pressure pipelines with axial flaws using constraint designed test specimens—part II: 3-D effects on constraint. Eng Fract Mech 2006;73:2123–38.
[43] Dowling AR, Townley CHA. The effects of defects on structural failure: a two-criteria approach. Int J Press Vessels Pip 1975;3:77–107.
[44] Harrinson RP, Loosemore K, Milne I. Assessment of the integrity of structures containing defects. CEGB report R-H-R6. UK: Central Electricity Generating Board; 1976.
[45] Folias ES. An axial crack in a pressurized cylindrical shell. International Journal of Fracture Mechanics 1965;1:104–13.